Structure of the translating *Neurospora* ribosome arrested by cycloheximide

Lunda Shen[a], Zhaoming Su[b,1], Kailu Yang[c,2], Cheng Wu[a], Thomas Becker[d], Deborah Bell-Pedersen[a], Junjie Zhang[c], and Matthew S. Sachs[a,3]

[a]Department of Biology, Texas A&M University, College Station, TX 77843; [b]Department of Bioengineering, Stanford University, Stanford, CA 94305; [c]Department of Biochemistry and Biophysics, Texas A&M University, College Station, TX 77843; and [d]Department of Biochemistry, Gene Center, Ludwig-Maximilians University Munich, 80539 Munich, Germany

Edited by Joseph D. Puglisi, Stanford University School of Medicine, Stanford, CA, and approved October 26, 2021 (received for review June 28, 2021)

Ribosomes translate RNA into proteins. The protein synthesis inhibitor cycloheximide (CHX) is widely used to inhibit eukaryotic ribosomes engaged in translation elongation. However, the lack of structural data for actively translating polyribosomes stalled by CHX leaves unanswered the question of which elongation step is inhibited. We elucidated CHX's mechanism of action based on the cryo-electron microscopy structure of actively translating *Neurospora crassa* ribosomes bound with CHX at 2.7-Å resolution. The ribosome structure from this filamentous fungus contains clearly resolved ribosomal protein eL28, like higher eukaryotes but unlike budding yeast, which lacks eL28. Despite some differences in overall structures, the ribosomes from *Neurospora*, yeast, and humans all contain a highly conserved CHX binding site. We also sequenced classic *Neurospora* CHX-resistant alleles. These mutations, including one at a residue not previously observed to affect CHX resistance in eukaryotes, were in the large subunit proteins uL15 and eL42 that are part of the CHX-binding pocket. In addition to A-site transfer RNA (tRNA), P-site tRNA, messenger RNA, and CHX that are associated with the translating *N. crassa* ribosome, spermidine is present near the CHX binding site close to the E site on the large subunit. The tRNAs in the peptidyl transferase center are in the A/A site and the P/P site. The nascent peptide is attached to the A-site tRNA and not to the P-site tRNA. The structural and functional data obtained show that CHX arrests the ribosome in the classical PRE translocation state and does not interfere with A-site reactivity.

translation | protein synthesis | cryo-electron microscopy

Cycloheximide (CHX) is the most widely used laboratory inhibitor of eukaryotic protein synthesis (1). Alma J. Whiffen, a mycologist working at Upjohn, initially identified it in 1946 as a product of *Streptomyces griseus* fermentation that she named actidione (diketone produced by an actinomycete); actidione inhibited the growth of fungi but not bacteria (2–4). In 1963, CHX's function to inhibit eukaryotic protein synthesis was demonstrated using a cell-free translation system (CFTS) from *Saccharomyces pastorianus* (5). The first induced mutations conferring CHX resistance were isolated and genetically mapped in the model fungus *Neurospora crassa* (6). Around 2 y later, the direct action of CHX to inhibit translation in a mammalian system was demonstrated using active translation lysates prepared from anucleate rabbit reticulocytes (7). The early literature on CHX and related molecules has been thoroughly and contemporaneously reviewed (8).

Structures of the *Saccharomyces cerevisiae* ribosome (9) and the human ribosome (10), containing CHX tightly bound at the ribosome E site, have given significant insight into its mechanism of action. Based on the position of the CHX binding site, CHX is proposed to interfere with the translocation of P-site transfer RNA (tRNA) to the E site. However, both of these CHX-containing structures were obtained using vacant ribosomes lacking tRNA and therefore did not establish the specific step(s) in the translation cycle at which CHX inhibits elongation. If E-site translocation is blocked as predicted, then this structure is consistent with ribosomes in the pretranslocation (PRE) state with either the nascent peptide on the P-site tRNA and the incoming amino acid on A-site tRNA or in the PRE state with the nascent peptide transferred to A-site tRNA. Both models appear in the literature, with single-molecule biophysical studies supporting the latter (1, 11). Furthermore, the ribosome subunits can have different, relative rotational orientations even while containing A/A and P/P tRNA: A classical PRE state can be discriminated from a rotated PRE* state (12). Thus, there are a variety of states in which CHX could potentially arrest the ribosome even prior to tRNA translocation.

Here, we determined the cryo-electron microscopy (cryo-EM) structure of translating *N. crassa* ribosomes with CHX at 2.7-Å resolution. To accomplish this, we isolated polysomes from actively growing cells to which CHX was added and maintained CHX at a high concentration throughout all subsequent procedures until the vitrification step of cryo-EM sample preparation. We built a model for the *N. crassa* ribosome that differs from *S. cerevisiae* ribosomes and more closely resembles higher-eukaryotic ribosomes in that it contains ribosomal protein eL28. Comparisons of structures with CHX bound to ribosomes showed that the CHX-binding position is highly conserved in *N. crassa*, *S. cerevisiae*, and human ribosomes. However, unlike

Significance

The ribosome has the central role in the translation of RNA. The elongation function of most eukaryotic ribosomes is arrested by the drug cycloheximide (CHX). The site of CHX binding is known. In this work, we determine the structure of a translating ribosome of a filamentous fungus arrested by CHX. By doing so, the specific state of the ribosome arrested in translation is revealed. This work is significant because it provides a structural basis to establish CHX's mechanism of action. It provides a model for a fungal ribosome and insights into the structure and function of eukaryotic ribosomes through comparative analyses of its features with those from other species.

Author contributions: L.S., Z.S., K.Y., C.W., T.B., D.B.-P., J.Z., and M.S.S. designed research; L.S., Z.S., K.Y., C.W., and M.S.S. performed research; L.S., Z.S., K.Y., C.W., T.B., D.B.-P., J.Z., and M.S.S. analyzed data; and L.S., Z.S., K.Y., C.W., T.B., D.B.-P., J.Z., and M.S.S. wrote the paper.

The authors declare no competing interest.

This article is a PNAS Direct Submission.

[1] Present address: The State Key Laboratory of Biotherapy and Cancer Center, Department of Geriatrics and National Clinical Research Center for Geriatrics, West China Hospital, Sichuan University, Chengdu, Sichuan 610044, China.

[2] Present address: Department of Molecular and Cellular Physiology, Stanford University School of Medicine, Stanford, CA 94305.

[3] To whom correspondence may be addressed. Email: msachs@bio.tamu.edu.

This article contains supporting information online at http://www.pnas.org/lookup/suppl/doi:10.1073/pnas.2111862118/-/DCSupplemental.

the canonical CHX-bound structures of vacant yeast and human ribosomes (9, 10), which contained an Mg^{2+} ion adjacent to the CHX-binding pocket, the *N. crassa* ribosome contained spermidine (SPD) in place of the Mg^{2+} ion. We sequenced previously identified *N. crassa* mutations that confer CHX resistance. All amino acid changes in these mutants, including an amino acid change at a previously unidentified position among eukaryotic mutations that confer CHX resistance, map to conserved residues in the CHX-binding pocket. In addition, P/P- and A/A-site tRNAs were present in the *N. crassa* structure, and the nascent peptide was resolved on the A-site tRNA. Finally, CHX did not appear to interfere with termination as it does with elongation in an *N. crassa* cell-free translation extract, consistent with CHX interfering with the translocation of tRNA to the E site but not peptidyl transfer events at the A site. The observation that terminating ribosomes are not arrested by CHX could be significant for analyses of the levels of ribosomes mapping to termination codons when CHX is included in ribosome-profiling analyses.

This work provides a structural basis for a mechanistic understanding of CHX action. It also provides a high-resolution model for a fungal ribosome that differs from the *S. cerevisiae* ribosome.

Results

Overall *N. crassa* Ribosome Structure. The original structures of eukaryotic ribosomes containing CHX were obtained using X-ray crystallography or cryo-EM by adding CHX to nontranslating vacant ribosomes (9, 10). Here, we obtained structures of actively translating ribosomes inhibited by CHX from the filamentous fungus *N. crassa* using cryo-EM and the workflow outlined in *SI Appendix*, Fig. S1. CHX was added to growing *N. crassa* cells, and clarified extracts were prepared, layered, and fractionated on sucrose gradients. Ribosomes were collected from the polysome-containing region of the gradients (*SI Appendix*, Fig. S1*A*) and prepared for cryo-EM imaging. CHX reversibly binds to ribosomes (13); therefore, we sought to maximize CHX association with ribosomes throughout the isolation and imaging procedures. To accomplish this, we added a high concentration of CHX (2 mg/mL) to the growth medium to arrest translation in vivo and maintained this concentration of CHX at all subsequent steps to obtain samples on grids for imaging.

The cryo-EM map of the 80S ribosome at an overall resolution of 2.7 Å (*SI Appendix*, Fig. S1 *C* and *D*) was determined using the approach in *SI Appendix*, Fig. S1*B*. We modeled *N. crassa* ribosomal RNAs (rRNAs) and ribosomal proteins and fitted them into the cryo-EM map (Fig. 1 and *SI Appendix*, Fig. S1*E* and Tables S1 and S2). This model of the *N. crassa* 80S ribosome included 93.6% of 26S, 100% of 5S, 100% of 5.8S, 98.5% of 18S rRNA nucleotides, 42 ribosomal proteins in the large subunit (LSU), and 32 ribosomal proteins in the small subunit (SSU). Heterogeneity of 5S rRNAs has been shown in *N. crassa* (14); the 5S rRNA model in our structure is based on the major α 5S rRNA sequence. As is seen with other 80S eukaryotic ribosome structures, *N. crassa* CPC-2 (15), the homolog of RACK1/ASC1, a nonribosomal protein, is stably associated and similarly positioned on the 40S subunit (Fig. 1). The *N. crassa* ribosome structure obtained also contains A-site and P-site tRNAs, CHX, SPD, and nascent peptide, as discussed below. Additionally, cryo-EM densities for 260 of the 269 Mg^{2+} ions identified in the *S. cerevisiae* ribosome structure 6T4Q (16) were confirmed in the *N. crassa* data. Finally, in this CHX-stalled conformation, regions of the ribosome corresponding to the P1 stalk and L1 stalk were not resolved, and therefore, uL10, uL11 (P1 stalk), and uL1 (L1 stalk) are not in the modeled structure.

We next compared the overall structure of the *N. crassa* ribosome to *S. cerevisiae* ribosomes (*SI Appendix*, Fig. S2*A*) and human ribosomes (*SI Appendix*, Fig. S2*B*). *N. crassa* and *S. cerevisiae* ribosomes are overall similar except for a striking difference at the top of the LSU (*SI Appendix*, Fig. S2*A*), comprising rRNA expansion segments $ES7^L$, $ES15^L$, and ribosomal protein eL6 (17, 18). Here, the *N. crassa* ribosome, like the human ribosome, contains ribosomal protein eL28, while the *S. cerevisiae* ribosome does not (*SI Appendix*, Fig. S2*A* and Movie S1). *N. crassa* eL28 is encoded by NCU06210, which is annotated as a hypothetical protein in the National Center for Biotechnology Information Database (NCBI Gene ID: 3879074). The interaction of *N. crassa* $ES7^L$ with eL28 is similar to that in the human ribosome (*SI Appendix*, Fig. S3 *A* and *B*). We looked at this difference between the fungal ribosomes more closely. Most Saccharomycotina, including *S. cerevisiae* and *Kluyveromyces lactis*, lack an eL28 gene, and there is no such protein in these two yeasts' ribosome structures (*SI Appendix*, Fig. S3 *C* and *D*). The structured region of the rRNA near *N. crassa* and human eL28 is not structured in purified *S. cerevisiae* and *K. lactis* ribosomes (*SI Appendix*, Fig. S3 *A–D*). However, the rRNAs from these yeasts contain the corresponding sequences. Interestingly, while *S. cerevisiae* ES7 is unstructured in this region in the absence of additional factors (*SI Appendix*, Fig. S3*C*), when the ribosome is associated with NatA (19), a protein complex that binds at the ribosome exit pore (*SI Appendix*, Fig. S3*E*), ES7 adapts a different structure which is closer to the *N. crassa* ES7 structure (*SI Appendix*, Fig. S3 *F* and *G*). An additional difference between the *N. crassa* and *S. cerevisiae* structures is that the *S. cerevisiae* ribosome contains density that corresponds to a structured L1 stalk and eIF5A (the large, orange-shaded area in the *S. cerevisiae* ribosome left view, *SI Appendix*, Fig. S2*A*), while *N. crassa* does not. Finally, the most striking differences between the *N. crassa* and human ribosomes (*SI Appendix*, Fig. S2*B*) are that human ribosomal rRNAs contain longer expansion segments than fungal rRNAs that can contribute to the structure (17).

Localization of CHX in the *N. crassa* Ribosome. We observed well-resolved, extra density for CHX near the E site of the LSU (Fig. 2 *A* and *B* and *SI Appendix*, Fig. S4*A*). CHX is located in a region demarcated by eL42, conserved 26S rRNA residues, and uL15. Comparison of the position of CHX in the *N. crassa* ribosome with its positions in the *S. cerevisiae* and human ribosomes reveals strong conservation of its orientation in the ribosome and the rRNA and ribosomal proteins surrounding it (Compare Fig. 2 *B–D*).

Importantly, additional density was present close to the *N. crassa* CHX binding site. We identified it as SPD (Fig. 2 *A* and *B* and *SI Appendix*, Fig. S5*A*). SPD was also recently modeled in a similar site in the submitted structure of the *S. cerevisiae* ribosome containing bound CHX and eIF5A (Protein Data Bank [PDB] ID: 6TNU, ref. 20) (*SI Appendix*, Fig. S5*B*). In cryo-EM maps of human ribosomes containing CHX, modeled Mg^{2+} or unmodeled SPD appear to be present (*SI Appendix*, Fig. S5 *C* and *D*) (10, 21). In other structures of human and *S. cerevisiae* ribosomes containing E/E-site or P/E-site tRNA (16, 21), unmodeled SPD is also present in a similar position (*SI Appendix*, Fig. S5 *E* and *F*). Thus, SPD binding to this region of the eukaryotic ribosome near the CHX binding site appears to be a common feature. Its structural and functional role(s), which remain to be determined, may well be of interest given its close vicinity to such an important functional site of the ribosome.

The comparisons of ribosomes containing CHX and containing E-site tRNA (*SI Appendix*, Fig. S5) support the proposed functional role of CHX to prevent the binding of deacylated tRNA (9, 10). CHX would clash with tRNA as the tRNA entered the E site upon transition from the P/P into the hybrid P/E position after peptidyl transfer.

***N. crassa* Mutations that Cause CHX Resistance Map to the CHX Binding Site.** CHX-resistant alleles of two identified genes that confer CHX resistance were obtained from the Fungal

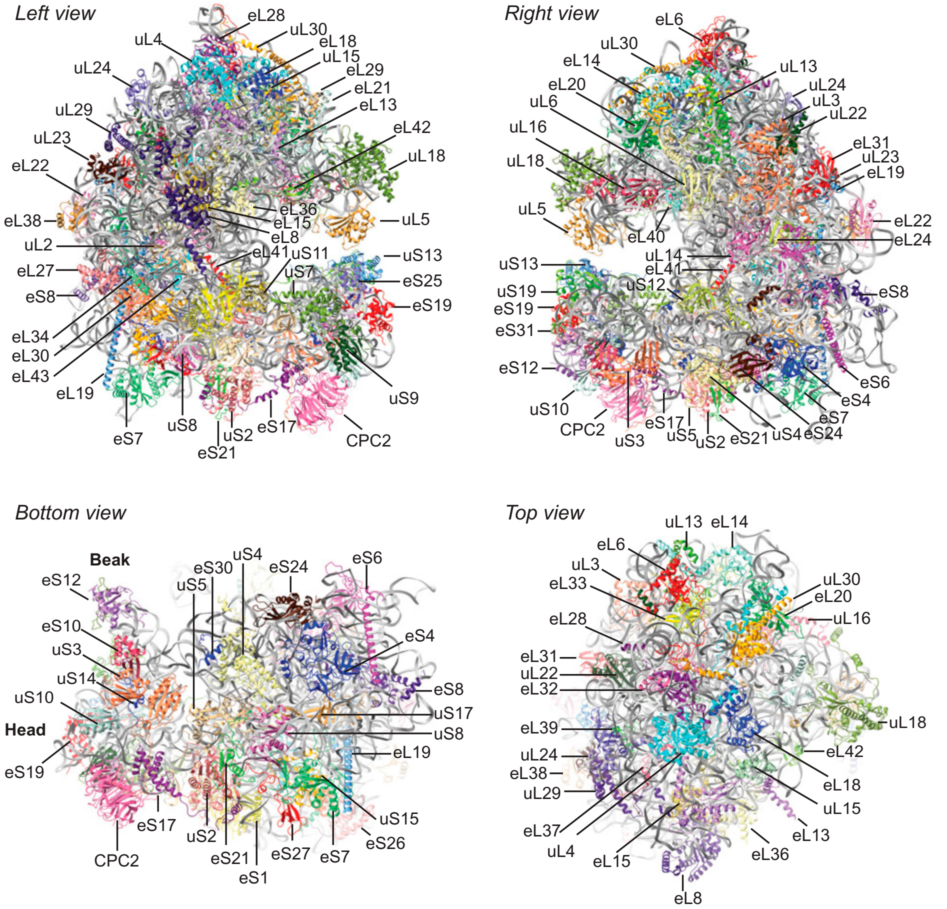

Left view

Right view

Bottom view

Top view

Fig. 1. Positions of *N. crassa* proteins associated with the 80S *N. crassa* ribosome. *N. crassa* proteins were fitted to the *N. crassa* cryo-EM map as described in the text. Left and right views are rotated 180° as are top and bottom views. Proteins are individually colored; rRNAs are all gray. Models for tRNAs, mRNA, CHX, SPD, Mg^{2+}, and nascent peptide are not shown.

Genetics Stock Center. Three alleles of *cyh-1* (NCU00706) and two alleles of *cyh-2* (NCU03806) were sequenced (*SI Appendix*, Table S3). The *cyh-1* mutations, which affect eL42, were P56L (two independent alleles) and F58L. The two alleles of *cyh-2* are two different mutations of the same residue in uL15: Q38K and Q38L. Like ribosomal mutations in *S. cerevisiae* and other organisms that result in CHX resistance, these mutations are close to the CHX binding site; the affected residues are indicated in red in Fig. 2. In addition, one of these residues identified by mutations in *N. crassa* and *S. cerevisiae*, uL15 Q38, and another residue identified in *S. cerevisiae*, H39 (22), are also in close proximity to SPD (Fig. 2 and Movie S2). All of the *N. crassa* mutants were more resistant to CHX than the wild-type in vivo (*SI Appendix*, Fig. S6) and in CFTSs derived from these strains (*SI Appendix*, Fig. S7*A*). In contrast, mutant and wild-type CFTSs were similarly sensitive to hygromycin B (HYG) (*SI Appendix*, Fig. S7*B*), an aminoglycoside translation inhibitor that binds near the ribosome A site (23), consistent with CHX and HYG targeting different regions of the LSU. These data, including the identification of a new mutation at a conserved residue that affects CHX resistance (F58L) and that maps to the CHX binding site, highlight the importance of the specific amino residues in this region for modulating the sensitivity of these ribosomes to inhibition by CHX.

The Positions of tRNAs, Nascent Peptide, Messenger RNA, and Ribosome Components Show that CHX-Arrested Ribosomes Are in the Classical PRE Translocation State. The structure of the CHX binding site is highly conserved in eukaryotic ribosomes. Ribosomes go through many different conformations during the various steps in the elongation cycle (12). At what step(s) does CHX inhibit elongation? We could answer this question by analyses of the peptidyltransferase center in the *N. crassa* ribosome structure. The CHX–ribosome structure determined here differs from previously published CHX-containing structures obtained from vacant ribosomes to which CHX was added (9, 10) and from subsets of translating ribosomes that contained CHX but were affinity-purified based on some other distinguishing feature (20, 21). The structure of the *N. crassa* ribosome containing CHX shows A/A- and P/P-site tRNAs (Fig. 3*A*). We wanted to know whether any subclass(es) of these ribosomes had tRNA in hybrid or other states, since mammalian ribosomes purified with CHX were observed to be in three major classes: classical–PRE, hybrid–PRE, and POST (posttranslocation) (21). Therefore, we did a three-dimensional (3D) classification of these particles into 10 subclasses. Every subclass had A/A- and P/P-site tRNA, and none had P/E- or A/P-site hybrid tRNA (*SI Appendix*, Fig. S8). These data indicated that the purification procedure we used maintained ribosomes in a CHX-arrested, classical PRE state.

No specific tRNAs are represented in the peptidyltransferase centers of polysomal ribosomes. Therefore, we adapted the tRNA model for a eukaryotic ICG–anticodon tRNA that decodes Arg codons (PDB ID: 6T4Q) (16) to model the tRNA densities of both A- and P-site tRNAs. Fitting the models to the tRNA densities allowed visualization of both A-site and P-site tRNAs in the peptidyltransferase center (Fig. 3*A*) and visualization of A-site and P-site messenger RNA (mRNA)–tRNA codon–anticodon interactions (Fig. 3 *B* and *C*). Importantly, we observed extra

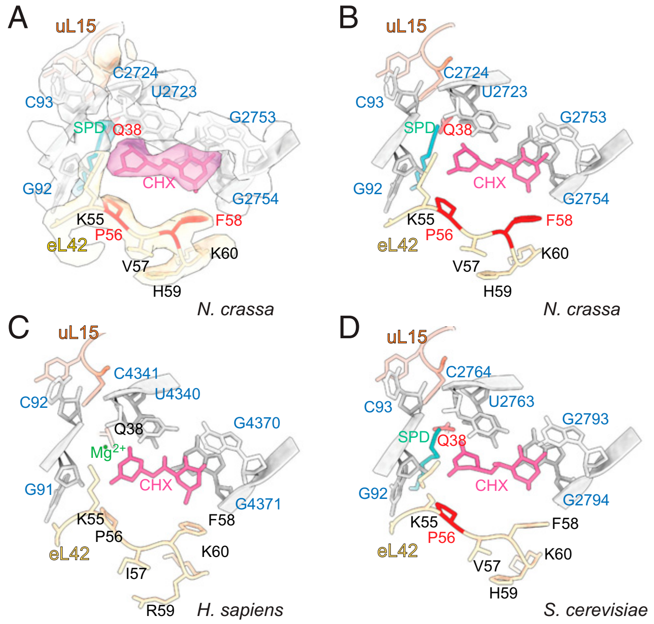

Fig. 2. CHX and SPD are both present in the *N. crassa* ribosome E site in actively translating ribosomes arrested by CHX. (*A*) Densities corresponding to CHX, SPD, and nearby *N. crassa* ribosomal components are indicated as surfaces and models as sticks and ribbons. (*B–D*) Comparisons of models of CHX and SPD or Mg^{2+} in the translating *N. crassa* ribosome (*B*); translating *S. cerevisiae* ribosome (*C*) (PDB ID: 6TNU); vacant human ribosome (*D*) (PDB ID: 5LKS). CHX is fuchsia; SPD is cyan; rRNA is gray; and eL42 and uL15 are yellow and orange, respectively, with residues at which mutations in the corresponding organism are known to result in CHX-resistance shaded red.

density corresponding to the nascent peptide attached to the 3′-hydroxyl group of the A-site tRNA but not the P-site tRNA (Fig. 3*A*). The map's local resolution at the position of this peptide–tRNA bond was ∼2.6 Å (*SI Appendix*, Fig. S4*B*). The density corresponding to the nascent peptide was not fully modeled because of the presence of many different nascent peptide species and nascent peptide conformations in polysomes. In contrast to the limited resolution of nascent peptide density, the density corresponding to the ribosome exit tunnel, including the constriction site important for nascent peptide interactions with the ribosome, could be confidently modeled (*SI Appendix*, Fig. S9).

The positions of the A/A- and P/P-site tRNAs and the nascent peptide's attachment to the A-site tRNA indicated that the *N. crassa* ribosome arrested by CHX is in the PRE state. Several conformations of the PRE state in human ribosomes can be discriminated by the relative orientations of the SSU and LSU and the positions of tRNAs (12). The conformation of the *N. crassa* ribosome with CHX (Fig. 4*A*), assessed by comparing the relative SSU–LSU configurations, better resembled the human classical-1 PRE state determined in the absence of CHX (Fig. 4*B*) than the rotated PRE* state (Fig. 4*C*).

Additional structural analyses support the assignment of the CHX-stalled *N. crassa* ribosome to the classical PRE state. Recently, the C-terminal tail of human uS19 was shown to change conformation depending on the functional state of the ribosome (21). This uS19 domain is positioned between the A- and P-site tRNAs near the anticodon–codon interaction with mRNA. Consistent with the *N. crassa* ribosome assignment to the classical PRE state, the position of *N. crassa* uS19 C-terminal tail in the CHX-stalled conformation is highly similar to the human uS19 in the classical PRE conformation (Fig. 4 *D* and *E*). These regions of *N. crassa* and human uS19 share identical amino acid sequences, while the *S. cerevisiae* uS19 C-terminal tail differs in sequence (*SI Appendix*, Fig. S10*A*). When comparing uS19 structures in *N. crassa*, human, and *S. cerevisiae* ribosomes containing CHX, all three uS19 structures are similar, except that the *S. cerevisiae* model lacks this C-terminal tail (*SI Appendix*, Fig. S10*B*). Thus, the A- and P-site tRNAs, uS19, and CHX are similarly positioned in the *N. crassa* and human structures, based on both models and cryo-EM maps, showing that CHX-bound ribosomes in both species are in the classical PRE state. However, unlike the case for the *N. crassa* ribosome, we do not see density corresponding to the nascent peptide on the A-site tRNA in the corresponding cryo-EM map for the mammalian, classical PRE ribosome (EMD-10668) (21), possibly because the peptide is disordered.

In conclusion, the structural data indicate that the CHX-arrested, translating *N. crassa* ribosome is in the classical-1 PRE state with the nascent peptide transferred to the A-site tRNA.

CHX Does Not Inhibit a Translation Termination Event. CHX does not interfere with A-site reactivity during elongation since the nascent peptide is transferred to the A-site tRNA. Therefore, in the presence of CHX, termination should still occur since release factors enter the A site to cause chain termination, and chain termination does not require tRNA translocation (24). Analyses of the positions of ribosomes in fungal CFTSs by primer–extension inhibition (toeprint) assays demonstrated that adding CHX before adding RNA to the system results in stabilization of ribosomes with the initiation codons of open reading frames (ORFs) in the P site and the second ORF

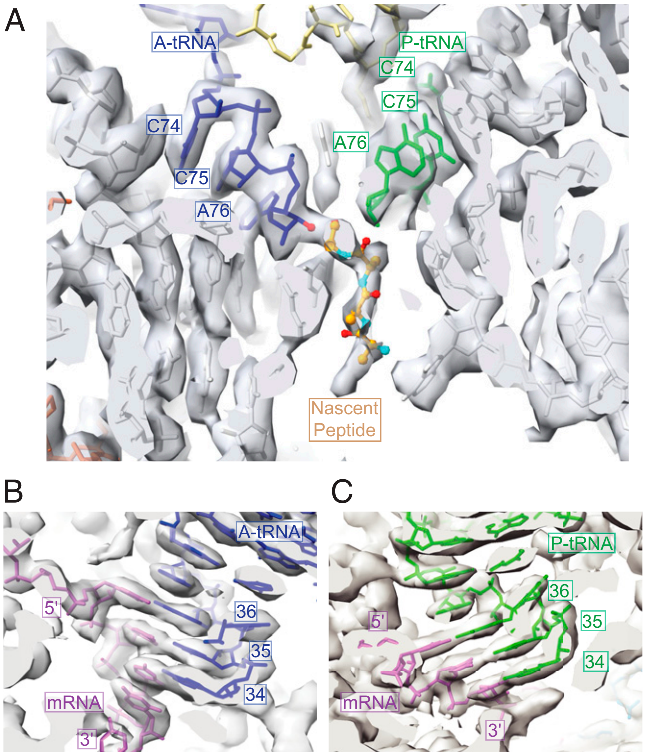

Fig. 3. CHX arrests ribosomes in the PRE translocation state with the nascent peptide attached to the A-site tRNA. (*A*) A- and P-site tRNAs at the peptidyltransferase center, with the nascent peptide attached to the A-site tRNA CCA end as shown by the EM density. (*B*) A-site tRNA anticodon interaction with the mRNA A-site codon. (*C*) P-site tRNA anticodon interaction with the mRNA P-site codon. A-site tRNA, blue; P-site tRNA, green; mRNA, purple; nascent peptide, various colors; rRNA, gray; uL16, yellow; and uL3, orange.

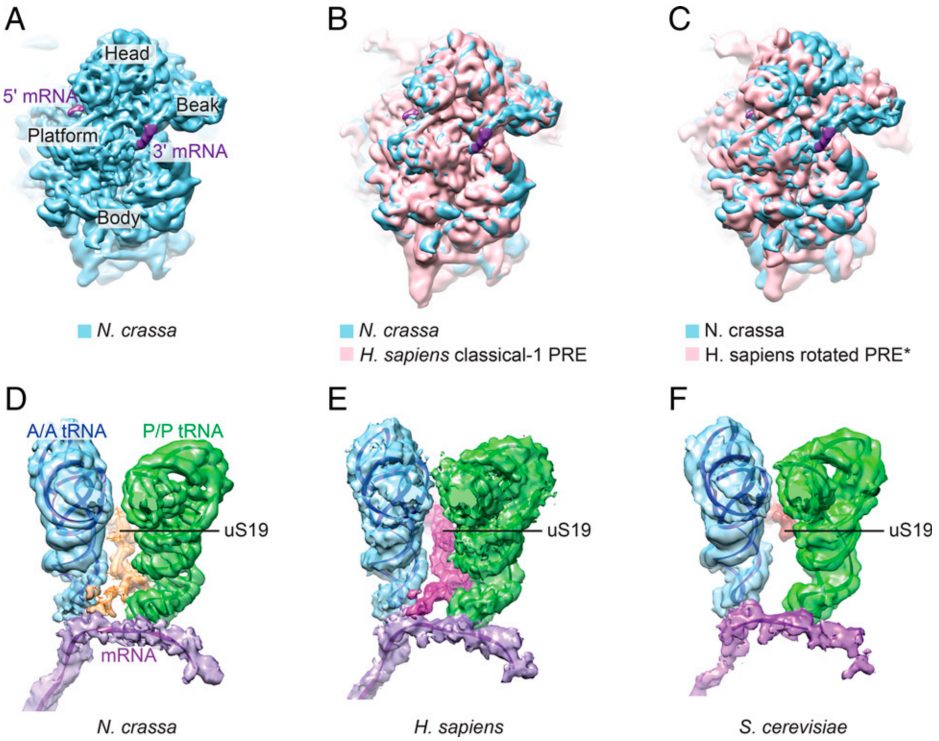

Fig. 4. The *N. crassa* CHX-bound ribosome is in the classical PRE state conformation. (*A*–*C*) Bottom view of the 80S ribosomes from *N. crassa* and *H. sapiens* low pass filtered to 10 Å for clarity. The 60S subunits are all aligned to the *N. crassa* 60S subunit. (*A*) The 40S subunit of *N. crassa* ribosome (blue). *N. crassa* mRNA is purple. (*B*) The 40S subunits of *N. crassa* ribosome (blue) and *H. sapiens* classical-1 PRE state ribosome (pink, EMD-2909) align well. (*C*) The 40S subunit of *H. sapiens* PRE* state ribosome (pink, EMD-2906) is rotated slightly counterclockwise compared to the 40S subunit of *N. crassa* ribosome (blue). (*D*–*F*) *N. crassa* uS19 (tan) and human uS19 (fuchsia) have similar contacts and conformations in the CHX-bound PRE state ribosome. The view given is similar to that in Bhaskar et al. (21) for comparison of the position of the uS19 C-terminal tail. The density of mRNA is low pass filtered to 10 Å for clarity, and the surface is displayed in purple. The C-terminal tails of both uS19 proteins interact with mRNA, A-site tRNA (blue), and P-site tRNA (green). (*D*) *N. crassa* uS19 position (tan) in the ribosome. (*E*) Human uS19 position (fuchsia) in the ribosome (EMD-10668, PDB ID: 6Y0G). tRNA densities were extracted from the cryo-EM map using ChimeraX. (*F*) *S. cerevisiae* uS19 position (rose) in the ribosome (EMD-10537, PDB ID: 6TNU).

codon in the A site (25). This is consistent with CHX causing elongation arrest at initiation codons. Toeprinting of CFTS translating RNA in the absence of CHX reveals the positions of ribosomes engaged in initiation, elongation, and termination (26). Early evidence that CHX does not interfere with termination was obtained using toeprinting to map the positions of ribosomes on mRNA in an *S. cerevisiae* CFTS (26). Since we had the structure of the *N. crassa* ribosome with CHX, we looked at the effect of CHX on termination kinetically using an *N. crassa* CFTS. We toeprinted ribosomes on a luciferase (LUC) reporter RNA with an upstream ORF (uORF) specifying the arginine attenuator peptide (AAP), which causes well-established, arginine-dependent transient stalling of ribosomes with a termination codon in the A site (27). If CHX did not inhibit termination, then ribosomes should be released from stalling through eventual, successful termination. However, if CHX inhibited termination, then the transient, Arg-dependent termination stall should be stabilized by CHX, as are elongation stalls. The results show that while CHX stabilizes ribosomes engaged in elongation (Fig. 5, indicated by arrowheads and brackets), it does not stabilize terminating ribosomes (Fig. 5, indicated by stars). Specifically, toeprint analyses of CFTS, to which CHX had been added for 0, 2.5, or 5 min, showed progressively decreased signals of ribosomes stalled at termination codons (Fig. 5, compare lanes 2, 3, and 4 and compare lanes 6, 7, and 8), consistent with termination occurring in its presence. Stalling of ribosomes at the AAP termination codon, which is Arg dependent, is most obvious when CFTS were analyzed immediately (0 min) after adding CHX (Fig. 5, compare lanes 2 and 6). In striking contrast, after 5 min in CHX, there was little difference in the signal from ribosomes at the AAP termination codon in low or high Arg (Fig. 5, compare lanes 4 and 8). This indicates that ribosomes at the termination codon are not stabilized by CHX. In contrast, toeprints corresponding to ribosomes engaged in elongation within the AAP-coding region, including those with the initiation codon in the ribosome P site, remained stable or increased during incubation with CHX, consistent with their expected stabilization by CHX.

Discussion

CHX is commonly used to inhibit eukaryotic translation and is an important reagent for ribosome-profiling analyses. Thus, it is crucial to understand its action during translation. Despite extensive biochemical work, however, CHX has only been studied from a structural perspective in the context of vacant 80S ribosomes (9, 10). Here, we focused on its action on translating ribosomes. We purified *N. crassa* ribosomes from polysome fractions isolated from cells in which translation was arrested by CHX and obtained their structure through single-particle cryo-EM. These data provide direct structural evidence that CHX's mechanism of action is to arrest ribosomes in the classical PRE state and do not support alternative models for its mechanism of action.

In *N. crassa* ribosomes containing CHX, the tRNAs are in the A/A and P/P sites, and there is no E-site tRNA. CHX has arrested these ribosomes in the classical PRE state with the nascent peptide attached to the A-site tRNA. The bases for assigning the CHX-arrested structure to the classical PRE state are as follows. First, the respective positions of the SSU and

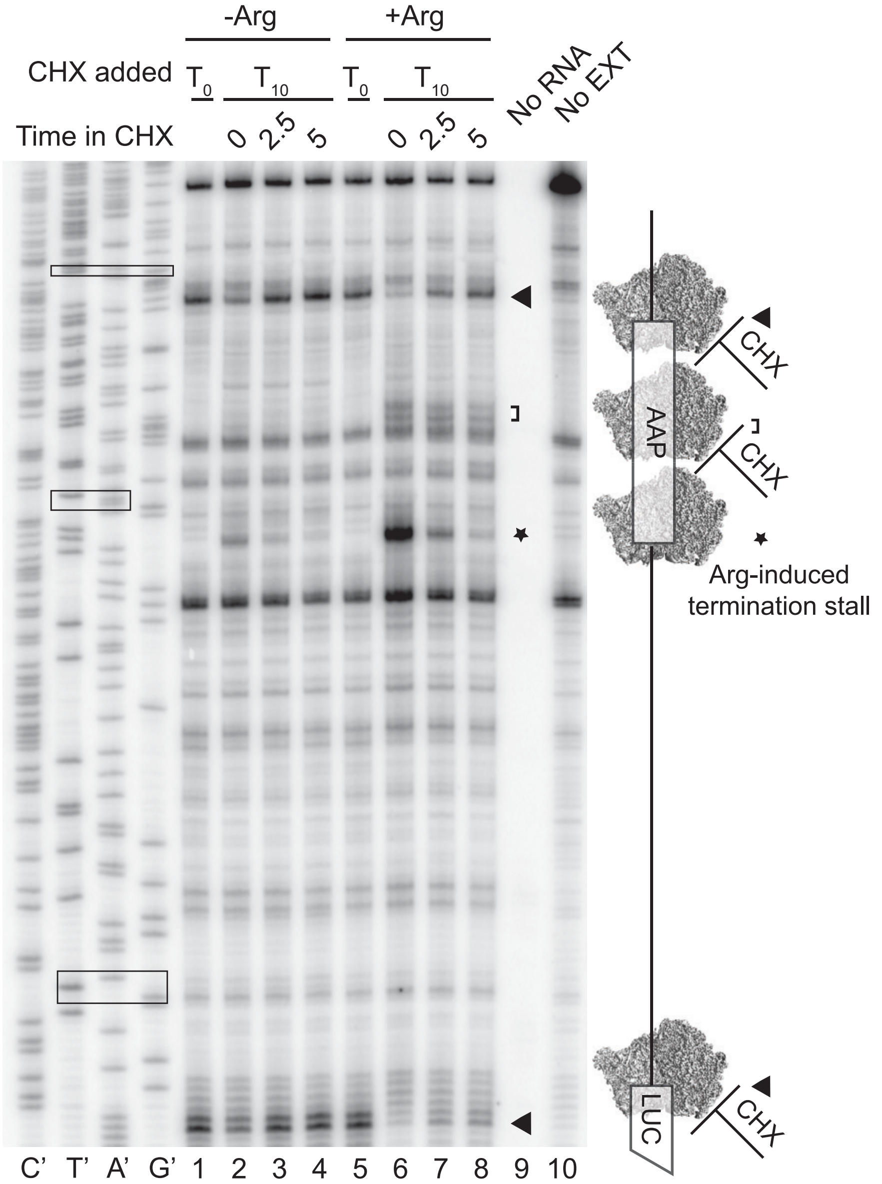

Fig. 5. Toeprinting shows that terminating ribosomes release from RNA in the presence of CHX but elongating ribosomes do not. In vitro synthesized, capped, and polyadenylated LUC reporter mRNA containing the wild-type AAP uORF was translated in the *N. crassa* CFTS in the presence of 10 μM (−) Arg or 2 mM (+) Arg (low or high Arg). CHX (final concentration 0.5 μg/μl) was added to the CFTS reactions either before the addition of mRNA (time T_0) or after translation was underway for 10 min (steady-state translation, time T_{10}). Steady-state reactions to which CHX was added were incubated in the presence of CHX for an additional 0, 2.5, or 5 min as indicated. The sequence of the mRNA can be directly deduced from the sequencing lanes reading from top to bottom. The positions of the uORF start and stop codons, and the LUC start codon, are boxed in the nucleotide sequence. The primer extension (toeprint) products corresponding to elongating ribosomes that have the uORF and LUC initiation codons in the P site are indicated by arrowheads; terminating ribosomes with the uORF termination codon in the A site are indicated with a star; and elongating ribosomes stalled within the uORF coding region are marked by a bracket. Control samples of RNA in reaction mixtures without extract and reaction mixtures containing extract but not mRNA are as indicated.

the LSU are most similar to the respective positions of human ribosomes in the classical-1 PRE state. Second, the uS19 C-terminal tail is resolved in the *N. crassa* structure and is in a conformation nearly identical to that of uS19 in human ribosomes in the classical PRE state. The classical PRE state is so far the only ribosome conformation for which this uS19 conformation has been observed (21). Furthermore, the *N. crassa* ribosome, like the human ribosome in the classical PRE state, does not contain eIF5A and has an unstructured L1 stalk. Also, consistent with arrest in the classical PRE state, the CHX-arrested *N. crassa* ribosome does not contain eEF2, which is associated with ribosomes in the process of translocation (12), or eEF1A, which is associated with POST-state ribosomes (28). This structural determination of the CHX-arrested state of ribosomes in polysomes as classical PRE with the peptide on the A-site tRNA is consistent with single-molecule biophysical data (11).

The use of high concentrations of CHX throughout the structural analysis procedure used here resulted in a population of ribosome particles that lacked any significant ribosome subpopulations containing tRNA in the P/E site. In contrast, in a study in which structural analyses followed purification of ribosomes with lower concentrations of CHX, which also included affinity purification steps, significant subpopulations of ribosomes lacking CHX and ribosomes with tRNAs in hybrid translocation states are also observed (21). Recent measurements of the dissociation constant of CHX from ribosomes yielded values of 1 ± 0.4 μM for *S. cerevisiae* ribosomes and 4 ± 1 μM for human ribosomes (29). A 1-μM dissociation constant corresponds to a half-life of 0.7 s for a first-order reaction (30). Because CHX binding is not irreversible, when it leaves, there is an increased kinetic chance of moving to the hybrid state occurring before CHX rebinding. The high concentrations of CHX we used could minimize these occurrences. The dissociation of CHX resulting in procession through the hybrid state could cause an additional round of elongation, which could be followed by subsequent CHX rebinding and arrest. Such considerations could be the basis for an alternative way to account for the proposed differences in CHX and lactimidomycin mechanisms of action that are distinct from mechanistic differences arising because of differences in the structures of these molecules (1).

The structure of CHX binding in translating *N. crassa* ribosomes is similar to the corresponding structures in vacant yeast and human ribosomes (9, 10). Thus, CHX is not altered by the presence of A/A- and P/P-site tRNA. Molecular analyses of the classical *N. crassa* CHX-resistant mutations (all of the alleles of *cyh-1* and *cyh-2* available from the Fungal Genetics Stock Center) showed that they affected residues at the binding site. Mutations at residues previously identified as important for CHX resistance were directly affected by some alleles: uL15 residue Q38 and eL42 residue P56. A mutation at an additional eL42 residue, F58L, was also discovered.

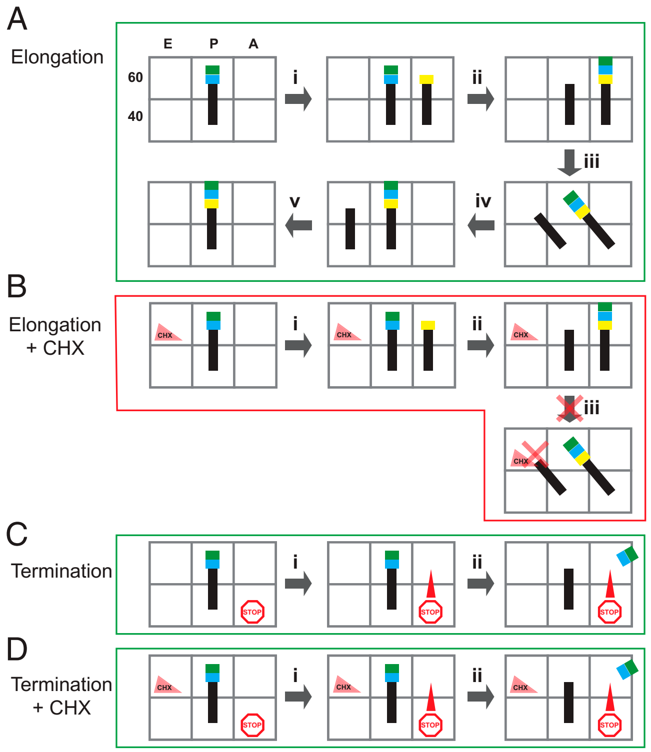

Fig. 6. Model for CHX action. E, P, and A sites of the 60S and 40S subunits are cartooned as open boxes; tRNAs are black lines; amino acids are blue, green, and yellow boxes; and CHX is a triangle in the 60S E site. (*A*) For a single-elongation cycle, in the absence of CHX, the aminoacyl-tRNA enters the empty A site (*i*), followed by nascent peptide transfer to the A-site tRNA (*ii*). Translocation occurs (*iii* and *iv*), and the deacylated tRNA leaves the E site to complete the cycle (*v*). (*B*) When CHX is bound in the E site, the aminoacyl-tRNA enters the empty A site (*i*), and transfer of the nascent peptide to the A-site tRNA occurs (*ii*). However, CHX in the E site prevents translocation of the P-site tRNA to the E site, arresting the ribosome in the PRE translocation state with the polypeptide attached to the A-site tRNA and deacylated tRNA in the P site. (*C*) For termination, a stop codon in the A site recruits release factor (*i*) resulting in release of the nascent peptide without translocation (*ii*). (*D*) When CHX is bound in the E site, termination occurs because translocation is not required.

These data can be integrated into the model initially proposed for CHX action, based on structural determination of its location in nontranslating (vacant) ribosomes in which CHX acts by clashing with occupancy of the E-site tRNA (9), but the structure of the translating ribosome's peptidyltransferase center was not known. Fig. 6 diagrams this integrated model for CHX action. Normally, in elongation (Fig. 6*A*), aminoacyl tRNA enters the A site (Fig. 6 *A*, *i*), and peptidyltransferase activity transfers the peptide to it from the P-site tRNA (Fig. 6 *A*, *ii*). Translocation of the tRNAs occurs (Fig. 6 *A*, *iii* and *iv*), and deacylated tRNA leaves the E site (Fig. 6 *A*, *v*). When CHX is in the E site (Fig. 6*B*), aminoacyl tRNA entry into the A site and transfer of the peptide onto the A-site aminoacyl tRNA occur (Fig. 6 *B*, *i* and *ii*), but translocation cannot happen. Therefore, the ribosome is arrested in the classical PRE state with the peptide on the A-site tRNA. Consistent with this model, our data indicate that CHX does not interfere with termination, because termination does not require translocation of tRNA (Fig. 6 *C* and *D*).

The loss of ribosomes with a termination codon in their A site from an mRNA in the continued presence of CHX, while ribosomes engaged in elongation on that mRNA are stabilized, has implications for assessing signals from terminating ribosomes in ribosome-profiling (ribo-seq) studies employing CHX to maintain ribosomes association with mRNA. The levels of ribosomes observed at termination codons could depend on differential effects of preparation and analysis conditions that do not have similar consequences for levels of ribosomes arrested during elongation because these latter ribosomes are generally stabilized by CHX.

We observed an additional density close to the *N. crassa* CHX binding site and unambiguously identified it as SPD (Fig. 2 *A* and *B* and *SI Appendix*, Fig. S5*A*). SPD is a polycation and is thought to function similarly to Mg^{2+}. Indeed, this SPD site is occupied by Mg^{2+} in the structure of the vacant human 80S ribosome bound with CHX (*SI Appendix*, Fig. S5*C*) and the vacant *S. cerevisiae* ribosome bound with CHX (9, 10). We sought to determine the generality of this finding of SPD instead of Mg^{2+}. SPD was recently modeled in the submitted structure of the *S. cerevisiae* ribosome containing bound CHX and eIF5A (20), and it is at the corresponding site (*SI Appendix*, Fig. S5*B*). While not modeled, densities for SPD at the corresponding sites are also present in *S. cerevisiae* ribosome without CHX but with E-site tRNA and human ribosomes with CHX or with E-site tRNA (*SI Appendix*, Fig. S5 *D*–*F*, respectively). These data, therefore, identify a conserved SPD binding site in eukaryotic ribosomes. It is worth noting that when we looked at 269 assigned Mg^{2+} binding sites in the *S. cerevisiae* ribosome in the *N. crassa* ribosome, we saw density corresponding to 260 of these Mg^{2+} molecules; in no case did we see density corresponding to SPD in these locations. Thus, while Mg^{2+} and SPD could potentially function interchangeably, it appears that the SPD binding site near the CHX binding site is different from other Mg^{2+} binding sites. In a published structure of rabbit 80S ribosome stalled on a poly(A) tail, two SPD molecules were provisionally included in the model (PDB ID: 6SGC) near the CCA 3′ end of P-site tRNA (31). However, we do not see corresponding densities in the *N. crassa* structure nor do we see density corresponding to SPD in the E site in this rabbit ribosome structure. Finally, some binding sites of SPD have been identified in high-resolution, prokaryotic ribosome structures [PDB ID codes: 7NHN (32), 4YBB (33), and 5IT8 (34)]. We compared these structures with the *N. crassa* ribosome structure and did not see densities for those SPD molecules in the corresponding regions of the *N. crassa* ribosome.

As is the case for the CHX-bound *N. crassa* ribosome, *S. cerevisiae* ribosomes that contain both CHX and eIF5A also have the nascent peptide attached to the A/A-site tRNA (20). However, in the presence of eIF5A, the L1 stalk is structured, and the E-site's structure, therefore, differs from that of the *N. crassa* ribosome. Furthermore, the C-terminal tail of uS19 is not resolved in this *S. cerevisiae* structure (Fig. 4*F*), consistent with the idea that a structured uS19 C-terminal tail, as observed in the *N. crassa* and human classical PRE ribosomes, is a distinct feature of that translational step. Thus, while there are similarities between the *N. crassa* and *S. cerevisiae* structures, as they each contain CHX, SPD, and nascent peptide on the A/A tRNA, these ribosomes are not in the same state. Therefore, the *S. cerevisiae* ribosome likely represents an eIF5A-specific state distinct from the classical PRE state seen in the presence of CHX alone.

This ribosome structure from the Ascomycete *N. crassa* represents a near atomic structure of a cytosolic ribosome from a filamentous fungus. The structure of the *N. crassa* mitochondrial ribosome was also recently determined (35). The structure of the *N. crassa* cytosolic ribosome differs from the Ascomycete yeast *S. cerevisiae* in that it contains eL28 while the yeast ribosome does not. Thus, as with the demonstration of the structure of a human-like translation factor eIF3 in *N. crassa* that is more complex than *S. cerevisiae* eIF3 (36) and the existence of mammalian-like, exon junction complex– mediated, nonsense-mediated mRNA decay in *N. crassa* that *S. cerevisiae* lacks (37, 38), this structure provides insight into important similarities and differences in the eukaryotic translational machinery. The 80S *K. lactis* ribosome structure (39) also lacks eL28; the yeast *K. lactis*, like *S. cerevisiae*, is a Saccharomycetes member. Interestingly, while eL28 is present in some protozoa, it is also missing in the ribosome structure from the protozoan *Trichomonas vaginalis* (18). How the loss of eL28 figures in these organisms' evolutionary history and the consequences of its presence versus absence for ribosome function are questions that remain to be answered.

In summary, we obtained the structure of the translating *N. crassa* ribosome arrested by CHX. This structure provides direct evidence that CHX arrests ribosomes in the classical PRE state with the nascent peptide on the A-site tRNA. The reactivity of the A site in the presence of CHX is also demonstrated by toeprinting analyses which showed that termination, unlike elongation, is not arrested by CHX. These studies also revealed that the *N. crassa* ribosome is structurally different from its budding yeast counterpart in containing eL28 and, in this respect, more closely resembles the ribosomes of mammals. Most fungi have eL28, and the *N. crassa* ribosome structure could be paradigmatic for these species, which include important Ascomycete pathogens such as *Aspergillus fumigatus* and Basidiomycete pathogens such as *Cryptococcus neoformans*. This work thus provides a structural basis for understanding CHX action and provides a model for these fungal ribosomes.

Materials and Methods

Strains and Culture Conditions. The *N. crassa* wild-type strain FGSC 2489 (74-OR23-1V A) and CHX-resistant *N. crassa* strains (*SI Appendix*, Table S3) were obtained from the Fungal Genetics Stock Center (40) and maintained as described (37, 41). Homokaryons of all strains were obtained by microconidiation (42).

Preparation, Analyses, and Purification of *N. crassa* Polysomes. *N. crassa* polysomes were prepared and analyzed, as previously described, with minor changes (43). Suspension of conidia was inoculated onto 50 mL solid Vogel's sucrose medium in a 250-mL flask. The culture was incubated at room temperature for 14 d, and conidia were harvested through two layers of cheesecloth. The number of conidia was counted, and the concentration was calculated. Conidia were inoculated to 500 mL Vogel's sucrose medium to make the final concentration of 1×10^7 conidia/mL, and the culture was incubated at 32 °C with orbital shaking (180 rpm). After about 6 h, when 90% of the conidia show germ tubes, CHX (2 mg/mL) was added to the culture 5 min before harvesting, and the germlings were harvested by vacuum filtration onto Whatman 541 filter paper. The mycelial pad was peeled off the filter paper and weighed. Mycelial pads (0.25 g each) were transferred to 2-mL screwcap tubes containing ice-cold 0.75 mL polysome extraction buffer (100 mM KCl, 20 mM Hepes-KOH [pH 7.5], 2 mM magnesium acetate, 15 mM 2-mercaptoethanol, and 2 mg/mL CHX) and 0.5 g zirconia/silica beads (0.5-mm diameter). The tubes were disrupted using a beadbeater at 4 °C for 50 s and centrifuged at $16,100 \times g$ at 4 °C for 5 min. Supernatants (0.45 mL) were transferred to fresh 2-mL screwcap tubes, frozen in liquid nitrogen, and stored at −80 °C.

For polysome analyses, 400 μL (about 18 A_{260} units) homogenate was layered on 12-mL linear sucrose gradients, which contain 10 to 50% (weight/weight) sucrose, 10 mM Hepes-KOH (pH 7.5), 70 mM ammonium acetate, 4 mM magnesium acetate, and 2 mg/mL CHX. Gradients were centrifuged using a Beckman SW41 rotor at 41,000 rpm at 4 °C for 2 h. BioComp Gradient Station Model 153 and Gilson Fraction Collector FC203B were used to generate the sucrose gradients and to analyze and fractionate the gradients, respectively. Polysome profiles were generated, and 26 fractions were collected from each gradient, flash frozen in liquid nitrogen, and stored at −80 °C.

Fractions corresponding to the polysomes (disomes and greater) from multiple gradients were pooled, washed, and concentrated using Corning Spin-X UF 6 mL Centrifugal Concentrators (100,000 molecular weight cut-off). The washing buffer was the buffer A that has been used to prepare *N. crassa* cell-free extract for in vitro translation [30 mM Hepes-KOH pH 7.6, 100 mM KOAc pH 7.0, 3 mM $Mg(OAc)_2$ pH 7.0, 2 mM DTT] supplemented with 2 mg/mL CHX. For each centrifugation, about 15 mL washing buffer was used, and the volume was concentrated to about 1 mL. The washing/concentrating was repeated six times to remove sucrose. Finally, the ribosomes were concentrated to about $A_{260} = 10$.

Cryo-EM Sample Preparation. Cryogrids were prepared as previously described (44). A total of 3 μL purified *N. crassa* polysomes was applied onto glow-discharged C-Flat 2/1 holey grids. The grids, equilibrated at 16 °C and 100% relative humidity, were plunged into liquid ethane to freeze them using a Vitrobot Mark III (FEI company).

Cryo-EM Single-Particle Data Acquisition. The frozen grids were loaded in a Titan Krios cryoelectron microscope (Thermo Fisher Scientific) operated at 300 kV, condenser lens aperture 50 μm, spot size 7, and parallel beam with an illuminated area of 1.08 μm in diameter. The nominal magnification was at 130,000×, corresponding to a calibrated sampling of 1.06 Å per physical pixel. Movie stacks were collected automatically using EPU software on a K2 direct electron camera equipped with a Bioquantum energy filter with an energy slit of 20 eV (Gatan), operating in counting mode at a recording rate of 5 raw frames/s and a total exposure time of 5 s, yielding 25 frames/stack, and a total dose of 32 e^-/Å^2. A total of 1,836 movie stacks were collected.

Cryo-EM Image Processing. All micrographs were imported into RELION-3.1 (45) for image processing. The motion correction was performed using MotionCor2 (46). The defocus and astigmatism were determined using CTFFIND4 (47). All particles were autopicked using the convolutional neural network–based script e2boxer.py in EMAN2 (48) and further checked manually to remove bad particles. After 2D classification in RELION-3.1, a total of 206,276 particles were subjected to 3D classification in RELION-3.1. The 3D classification of LSU and SSU was performed in RELION-3.1 to further remove bad particles. Then, a total of 196,154 particles were subjected to Bayesian polishing in RELION-3.1, followed by 3D reconstruction using cryo-SPARC (49). A sharpening B-factor of −65.4 Å^2 was applied to the resulting cryo-EM map to yield the final sharpened map at 2.7-Å global resolution estimated by the 0.143 criterion of the Fourier Shell Correlation (FSC) curve. Local resolution maps were determined in RELION-3.1.

Molecular Modeling. The sequences of *N. crassa* 5S, 5.8S, 18S, and 26S rRNA used to build the model were obtained through NCBI (GenBank IDs K02469.1, M10692.1, FJ360521.1, and FJ360521.1, respectively). Template-based comparative modeling was performed using modeRNA (50). The *S. cerevisiae* 80S structures (PDB ID codes: 4U3U and 6T4Q) (9, 16) were chosen as the templates. The sequences were aligned using the SILVA ACT website (https://www.arb-silva.de/aligner/) (51). The structures of the rRNA expansion segments were manually built using Rosetta (52) and Coot (53) with the aid of the secondary structures that were predicted by RNAfold WebServer (rna.tbi.univie.ac.at/cgi-bin/RNAWebSuite/RNAfold.cgi) (54). The rRNA structures were refined using Rosetta and PHENIX (55).

The sequences of *N. crassa* ribosomal proteins were obtained from the UniProt database. For each ribosomal protein, the initial homology model was generated using MODELER (56) and then refined into the cryo-EM map using Rosetta (52). The best model was then selected based on both the geometry and the fitting scores.

The tRNA model used for A- and P-site tRNAs was the eukaryotic ICG-anticodon tRNA that decodes Arg codons (PDB ID: 6T4Q) (16). The mRNA model and nascent peptide model were adapted from the mRNA model and nascent peptide model in a human classical PRE ribosome structure (PDB ID: 6Y0G) (21).

CHX and SPD modeling was done with the electronic Ligand Builder and Optimization Workbench (57). The models of Mg^{2+} ions were adapted from the *S. cerevisiae* ribosome structure [PDB ID: 6T4Q (16)].

The models of all rRNA, ribosomal proteins, tRNA, mRNA, nascent peptide, CHX, SPD, and Mg^{2+} were then merged into one model, refined using Rosetta and PHENIX and inspected and adjusted using Coot.

The statistics obtained by using PHENIX and MolProbity (58) of the refined 80S ribosome model are listed in *SI Appendix*, Table S4.

Structural Figures and Movies Preparation. All figures and movies were made using UCSF Chimera (59) and UCSF ChimeraX (60).

Sequencing of *N. crassa cyh-1* and *cyh-2* Alleles. Genomic DNA was isolated as described (43). For each strain, the DNA sequences of both *cyh-1* (NCU00706) and *cyh-2* (NCU03806) genes were determined by PCR amplification of genomic DNA, followed by sequencing of the PCR product. For *cyh-1*, oligo pair OLS041 (GACCTCACACATCAACGA)/OLS042 (TTCGCAACCTCGCTACCA) were used for amplification and sequencing and an additional oligo, OLS057 (TCATGTCGCGTCGAGCTCTGT), was also used for sequencing. For *cyh-2*, oligo pairs CYH2F1 (CGAGA CCCGTGAAGCGTCT)/CYH2R1 (TTGAGGATGGG GGCCCAC) and CYH2F2 (GACGATGACGGATAGACC)/CYH2R2 (GGCTTCTGGACGAATGTT) were used for both amplification and sequencing. The *cyh-1* sequencing reads were aligned to NCBI Reference Sequence, XM_959447.3, and the *cyh-2* sequencing reads were aligned to GenBank, AL513466.1 (which includes *cyh-2*), to identify the mutations.

Determination of CHX Resistance Levels In Vivo. For testing CHX resistance, conidia (10^4 in 50 μL sterile water) from wild-type and mutant strains were inoculated into 16 × 125-mm tubes containing 3 mL Vogel's minimal medium/2% sucrose/2% agar supplemented with CHX after autoclaving. Cultures were grown for 8 d at room temperature. Tubes were scored for growth and photographed.

Preparation of Cell-Free Translation Systems, Determination of CHX Resistance Levels In Vitro, and Toeprinting. The procedures for preparation of CFTS, preparation of in vitro–synthesized capped and polyadenylated LUC RNA for translation and for toeprinting without and with CHX were as previously described (26, 41). For testing CHX sensitivity and Hyg sensitivity, drugs at the indicated concentrations were added at T_0.

Data Availability. The Coulomb potential map and atomic coordinates have been deposited in the Electron Microscopy Databank (EMDB code: EMD-24307) (61) and PDB (PDB ID code: 7R81) (62). All other study data are included in the article and/or supporting information.

ACKNOWLEDGMENTS. We are grateful for cryo-EM support from Dr. Wah Chiu. Cryo-EM data were collected at the Stanford Linear Accelerator Center and Stanford under NIH grants (S10OD021600 and U24GM116787). This work was supported by grants NIH R35 GM126966 to D.B.-P., NIH regional cryo-EM data collection consortium U24GM1167 and Welch Foundation A1863 to J.Z., and NIH R21 AI138158 to M.S.S.

1. T. Schneider-Poetsch *et al.*, Inhibition of eukaryotic translation elongation by cycloheximide and lactimidomycin. *Nat. Chem. Biol.* **6**, 209–217 (2010).
2. A. J. Whiffen, N. Bohonos, R. L. Emerson, The production of an antifungal antibiotic by *Streptomyces griseus*. *J. Bacteriol.* **52**, 610–611 (1946).
3. B. E. Leach, J. H. Ford, A. J. Whiffen, Actidione, an antibiotic from *Streptomyces griseus*. *J. Am. Chem. Soc.* **69**, 474 (1947).
4. A. J. Whiffen, The production, assay, and antibiotic activity of actidione, an antibiotic from *Streptomyces griseus*. *J. Bacteriol.* **56**, 283–291 (1948).
5. M. R. Siegel, H. D. Sisler, Inhibition of protein synthesis in vitro by cycloheximide. *Nature* **200**, 675–676 (1963).
6. K. S. Hsu, The genetic basis of actidione resistance in *Neurospora*. *J. Gen. Microbiol.* **32**, 341–347 (1963).
7. B. Colombo, L. Felicetti, C. Baglioni, Inhibition of protein synthesis by cycloheximide in rabbit reticulocytes. *Biochem. Biophys. Res. Commun.* **18**, 389–395 (1965).
8. H. D. Sisler, M. R. Siegel, "Cycloheximide and other glutarimide antibiotics" in *Antibiotics 1: Mechanism of Action*, D. Gottlieb, P. D. Shaw, Eds. (Springer-Verlag, Berlin, Heidelberg, 1967), pp. 283–307.
9. N. Garreau de Loubresse *et al.*, Structural basis for the inhibition of the eukaryotic ribosome. *Nature* **513**, 517–522 (2014).
10. A. G. Myasnikov *et al.*, Structure-function insights reveal the human ribosome as a cancer target for antibiotics. *Nat. Commun.* **7**, 12856 (2016).
11. T. Budkevich *et al.*, Structure and dynamics of the mammalian ribosomal pretranslocation complex. *Mol. Cell* **44**, 214–224 (2011).
12. E. Behrmann *et al.*, Structural snapshots of actively translating human ribosomes. *Cell* **161**, 845–857 (2015).
13. F. O. Wettstein, H. Noll, S. Penman, Effect of cycloheximide on ribosomal aggregates engaged in protein synthesis in vitro. *Biochim. Biophys. Acta* **87**, 525–528 (1964).
14. E. U. Selker, J. N. Stevens, R. L. Metzenberg, Heterogeneity of 5S RNA in fungal ribosomes. *Science* **227**, 1340–1343 (1985).
15. F. Müller *et al.*, The *cpc-2* gene of *Neurospora crassa* encodes a protein entirely composed of WD-repeat segments that is involved in general amino acid control and female fertility. *Mol. Gen. Genet.* **248**, 162–173 (1995).
16. P. Tesina *et al.*, Molecular mechanism of translational stalling by inhibitory codon combinations and poly(A) tracts. *EMBO J.* **39**, e103365 (2020).
17. J.-P. Armache *et al.*, Cryo-EM structure and rRNA model of a translating eukaryotic 80S ribosome at 5.5-A resolution. *Proc. Natl. Acad. Sci. USA* **107**, 19748–19753 (2010).
18. Z. Li *et al.*, Cryo-EM structures of the 80S ribosomes from human parasites *Trichomonas vaginalis* and *Toxoplasma gondii*. *Cell Res.* **27**, 1275–1288 (2017).
19. A. G. Knorr *et al.*, Ribosome-NatA architecture reveals that rRNA expansion segments coordinate N-terminal acetylation. *Nat. Struct. Mol. Biol.* **26**, 35–39 (2019).
20. R. Buschauer *et al.*, The Ccr4-Not complex monitors the translating ribosome for codon optimality. *Science* **368**, eaay6912 (2020).
21. V. Bhaskar *et al.*, Dynamics of uS19 C-terminal tail during the translation elongation cycle in human ribosomes. *Cell Rep.* **31**, 107473 (2020).
22. A. M. McGeachy, Z. A. Meacham, N. T. Ingolia, An accessible continuous-culture turbidostat for pooled analysis of complex libraries. *ACS Synth. Biol.* **8**, 844–856 (2019).
23. M. A. Borovinskaya, S. Shoji, K. Fredrick, J. H. D. Cate, Structural basis for hygromycin B inhibition of protein biosynthesis. *RNA* **14**, 1590–1599 (2008).
24. C. U. T. Hellen, Translation termination and ribosome recycling in eukaryotes. *Cold Spring Harb. Perspect. Biol.* **10**, a032656 (2018).
25. A. Gaba, Z. Wang, T. Krishnamoorthy, A. G. Hinnebusch, M. S. Sachs, Physical evidence for distinct mechanisms of translational control by upstream open reading frames. *EMBO J.* **20**, 6453–6463 (2001).
26. C. Wu, N. Amrani, A. Jacobson, M. S. Sachs, "The use of fungal in vitro systems for studying translational regulation" in *Translation Initiation: Extract Systems and Molecular Genetics*, J. Lorsch, Ed. (Elsevier, San Diego, 2007), vol. **429**, pp. 203–225.
27. T. E. Dever, I. P. Ivanov, M. S. Sachs, Conserved upstream open reading frame nascent peptides that control translation. *Annu. Rev. Genet.* **54**, 237–264 (2020).
28. J. Flis *et al.*, tRNA translocation by the eukaryotic 80S ribosome and the impact of GTP hydrolysis. *Cell Rep.* **25**, 2676–2688.e7 (2018).
29. S. Pellegrino *et al.*, Understanding the role of intermolecular interactions between lissoclimides and the eukaryotic ribosome. *Nucleic Acids Res.* **47**, 3223–3232 (2019).
30. T. D. Pollard, A guide to simple and informative binding assays. *Mol. Biol. Cell* **21**, 4061–4067 (2010).
31. V. Chandrasekaran *et al.*, Mechanism of ribosome stalling during translation of a poly(A) tail. *Nat. Struct. Mol. Biol.* **26**, 1132–1140 (2019).
32. C. Crowe-McAuliffe *et al.*, Structural basis of ABCF-mediated resistance to pleuromutilin, lincosamide, and streptogramin A antibiotics in Gram-positive pathogens. *Nat. Commun.* **12**, 3577 (2021).
33. J. Noeske *et al.*, High-resolution structure of the *Escherichia coli* ribosome. *Nat. Struct. Mol. Biol.* **22**, 336–341 (2015).
34. A. I. Cocozaki *et al.*, Resistance mutations generate divergent antibiotic susceptibility profiles against translation inhibitors. *Proc. Natl. Acad. Sci. U.S.A.* **113**, 8188–8193 (2016).
35. Y. Itoh, A. Naschberger, N. Mortezaei, J. M. Herrmann, A. Amunts, Analysis of translating mitoribosome reveals functional characteristics of translation in mitochondria of fungi. *Nat. Commun.* **11**, 5187 (2020).
36. M. D. Smith *et al.*, Human-like eukaryotic translation initiation factor 3 from *Neurospora crassa*. *PLoS One* **8**, e78715 (2013).
37. Y. Zhang, M. S. Sachs, Control of mRNA stability in fungi by NMD, EJC and CBC factors through 3′UTR introns. *Genetics* **200**, 1133–1148 (2015).
38. A. Kurilla, A. Szőke, A. Auber, K. Káldi, D. Silhavy, Expression of the translation termination factor eRF1 is autoregulated by translational readthrough and 3'UTR intron-mediated NMD in *Neurospora crassa*. *FEBS Lett.* **594**, 3504–3517 (2020).
39. B. Y. Huang, I. S. Fernández, Long-range interdomain communications in eIF5B regulate GTP hydrolysis and translation initiation. *Proc. Natl. Acad. Sci. U.S.A.* **117**, 1429–1437 (2020).
40. K. McCluskey, A. Wiest, M. Plamann, The Fungal Genetics Stock Center: A repository for 50 years of fungal genetics research. *J. Biosci.* **35**, 119–126 (2010).
41. C. Wu, A. Dasgupta, L. Shen, D. Bell-Pedersen, M. S. Sachs, The cell free protein synthesis system from the model filamentous fungus *Neurospora crassa*. *Methods* **137**, 11–19 (2018).

42. D. Ebbole, M. S. Sachs, A rapid and simple method for isolation of *Neurospora crassa* homokaryons using microconidia. *Fungal Genet. Newsl.* **37**, 17–18 (1990).
43. Z. Luo, M. Freitag, M. S. Sachs, Translational regulation in response to changes in amino acid availability in *Neurospora crassa. Mol. Cell. Biol.* **15**, 5235–5245 (1995).
44. K. Yang *et al.*, Structural insights into species-specific features of the ribosome from the human pathogen *Mycobacterium tuberculosis*. *Nucleic Acids Res.* **45**, 10884–10894 (2017).
45. J. Zivanov *et al.*, New tools for automated high-resolution cryo-EM structure determination in RELION-3. *eLife* **7**, e42166 (2018).
46. S. Q. Zheng *et al.*, MotionCor2: Anisotropic correction of beam-induced motion for improved cryo-electron microscopy. *Nat. Methods* **14**, 331–332 (2017).
47. A. Rohou, N. Grigorieff, CTFFIND4: Fast and accurate defocus estimation from electron micrographs. *J. Struct. Biol.* **192**, 216–221 (2015).
48. G. Tang *et al.*, EMAN2: An extensible image processing suite for electron microscopy. *J. Struct. Biol.* **157**, 38–46 (2007).
49. A. Punjani, J. L. Rubinstein, D. J. Fleet, M. A. Brubaker, cryoSPARC: Algorithms for rapid unsupervised cryo-EM structure determination. *Nat. Methods* **14**, 290–296 (2017).
50. M. Rother, K. Rother, T. Puton, J. M. Bujnicki, ModeRNA: A tool for comparative modeling of RNA 3D structure. *Nucleic Acids Res.* **39**, 4007–4022 (2011).
51. E. Pruesse, J. Peplies, F. O. Glöckner, SINA: Accurate high-throughput multiple sequence alignment of ribosomal RNA genes. *Bioinformatics* **28**, 1823–1829 (2012).
52. F. DiMaio *et al.*, Atomic-accuracy models from 4.5-Å cryo-electron microscopy data with density-guided iterative local refinement. *Nat. Methods* **12**, 361–365 (2015).
53. P. Emsley, K. Cowtan, Coot: Model-building tools for molecular graphics. *Acta Crystallogr. D Biol. Crystallogr.* **60**, 2126–2132 (2004).
54. A. R. Gruber, R. Lorenz, S. H. Bernhart, R. Neuböck, I. L. Hofacker, The Vienna RNA websuite. *Nucleic Acids Res.* **36**, W70–W74 (2008).
55. P. D. Adams *et al.*, PHENIX: A comprehensive Python-based system for macromolecular structure solution. *Acta Crystallogr. D Biol. Crystallogr.* **66**, 213–221 (2010).
56. N. Eswar *et al.*, Comparative protein structure modeling using MODELLER. *Curr. Protoc. Protein Sci.* 10.1002/0471140864.ps0209s50 (2007).
57. N. W. Moriarty, R. W. Grosse-Kunstleve, P. D. Adams, electronic Ligand Builder and Optimization Workbench (eLBOW): A tool for ligand coordinate and restraint generation. *Acta Crystallogr. D Biol. Crystallogr.* **65**, 1074–1080 (2009).
58. C. J. Williams *et al.*, MolProbity: More and better reference data for improved all-atom structure validation. *Protein Sci.* **27**, 293–315 (2018).
59. E. F. Pettersen *et al.*, UCSF Chimera–A visualization system for exploratory research and analysis. *J. Comput. Chem.* **25**, 1605–1612 (2004).
60. T. D. Goddard *et al.*, UCSF ChimeraX: Meeting modern challenges in visualization and analysis. *Protein Sci.* **27**, 14–25 (2018).
61. L. Shen *et al.*, Structure of the translating *Neurospora crassa* ribosome arrested by cycloheximide. Electron Microscopy Data Bank. https://www.emdataresource.org/EMD-24307. Deposited 25 June 2021.
62. L. Shen *et al.*, Structure of the translating *Neurospora crassa* ribosome arrested by cycloheximide. Protein Data Bank. https://www.rcsb.org/structure/7R81. Deposited 25 June 2021.